ADVANCED FUNCTIONAL MATERIALS

www.afm-journal.de

Enhanced Second Harmonic Generation in Double-Resonance Colloidal Metasurfaces

*Yuan Zeng, Haoliang Qian, Matthew J. Rozin, Zhaowei Liu, and Andrea R. Tao**

A key challenge for optical circuits is the ability to integrate nonlinear optical signal processing components such as optical modulators and frequency mixers at the chip scale. Optical antennas that focus light into nanoscale volumes can be utilized to shrink the footprint and increase the efficiency of these components. Multiresonant antennas that enhance both optical absorption and emission process are recently demonstrated to enable efficient nonlinear frequency conversion at the nanoscale and are promising as structures for second harmonic generation (SHG) and upconversion. Here, the ability of colloidal metasurfaces fabricated by self-assembly as on-chip platforms for enhanced SHG is demonstrated. These metasurfaces exhibit high spatial overlap of multiple surface plasmon modes whose frequencies can be independently tuned through appropriate design of colloidal and metasurface geometries. It is demonstrated that these bottom-up structures rival lithographic nonlinear optical antennas in SHG efficiency, suggesting the potential for these colloidal metasurfaces in integrated on-chip architectures.

1. Introduction

Metallic nanostructures that support surface plasmons have been demonstrated to exhibit a wide range of nonlinear optical phenomena,[1,2] including enhanced second harmonic generation (SHG).[3–5] SHG is a nonlinear wave-mixing process where two incident photons at the same fundamental wavelength (λ_{FW}) combine to produce a single, higher energy photon at the second harmonic ($\lambda_{SH} = \lambda_{FW}/2$) wavelength. In bulk materials that possess a large nonlinear susceptibility[6] (χ^2) such as β-barium borate and lithium niobate, SHG stems from light–matter interactions with a non-centrosymmetric crystal lattice. SHG is also supported by under-coordinated surface structures due to centrosymmetric breakdown.[7–11] A major drawback with using surface-generated SHG, however, is a reduced nonlinear interaction length. Enhanced SHG overcomes this by taking advantage of metal surfaces that support the excitation of surface plasmon resonances (SPRs)[12,13] that can serve to enhance the near-field intensity[14–16] at either the fundamental or the second harmonic wavelengths.[2,17,18] However, it is difficult to match both optical excitation and emission by a structure that exhibits only a single plasmon resonance.

Double-resonance nanostructures can be designed to support two different types of optical modes (e.g., a Fabry–Perot-like resonance mode and an SPR mode),[19] similar types of resonance modes with different polarizations,[20] two separate optical components that each supports a resonance mode,[17,21–23] or multiresonance structures with either multiple components or branches.[24–29] The ability of these double-resonance structures to maximize re-emission into the far-field is highly promising for the development of nonlinear light sources. However, the majority of these designs require components that possess complex nanostructured architectures and precise control of the resonance frequencies, which determined by the size,[30] shape,[31,32] and orientation[33] of metal nanostructures. As a result, nanostructured metasurfaces supporting SHG have predominantly relied on direct-write or lithography-based nanofabrication techniques,[17,19,22,34,35] limiting the ability to generate large-scale arrays for light emission. While suitable for building proof-of-concept structures, such fabrication processes are not amenable to nanomanufacturing considerations such as scalability, throughput, and cost.

Plasmonic metasurfaces have the potential to serve as effective platforms for enhanced SHG because they can be designed to exhibit a double-resonance effect, with near-field enhancement occurring at both the fundamental and the second harmonic wavelengths. Here, we present a highly scalable, bottom-up approach to fabricating plasmonic metasurfaces for SHG and light emission. Colloidal nanocrystals assembled into periodic arrays serve as the foundation for ultrathin nonlinear optical metasurfaces that absorb in the near-infrared (IR) and emit in the visible. We observe SHG from a nanocube-on-metal structure similar to those first reported by Moreau et al.[36] Rozin et al. previously demonstrated that colloidal metasurfaces are capable of supporting multiple, spectrally separated but spatially overlapping plasmon resonances that induce

Y. Zeng, Dr. M. J. Rozin, Prof. A. R. Tao
Department of NanoEngineering
University of California, San Diego
MC 0448, 9500 Gilman Drive, La Jolla, CA 92093-0448, USA
E-mail: atao@eng.ucsd.edu

Y. Zeng, Dr. M. J. Rozin, Prof. Z. Liu, Prof. A. R. Tao
Materials Science and Engineering
University of California, San Diego
9500 Gilman Drive, La Jolla, CA 92093, USA

Dr. H. Qian, Prof. Z. Liu
Department of Electrical and Computer Engineering
University of California, San Diego
9500 Gilman Drive, La Jolla, CA 92093, USA

The ORCID identification number(s) for the author(s) of this article can be found under https://doi.org/10.1002/adfm.201803019.

DOI: 10.1002/adfm.201803019

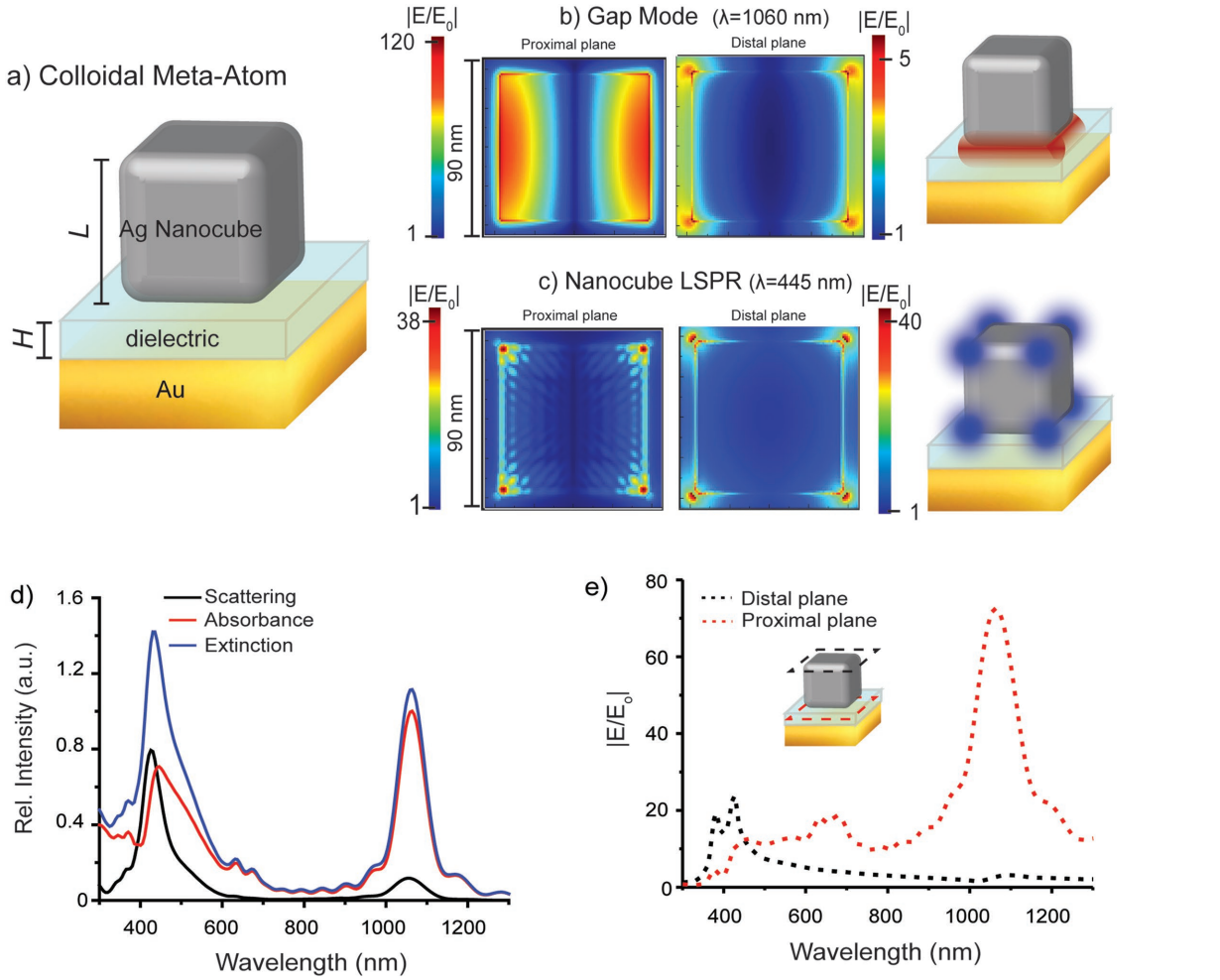

Figure 1. Schematic and simulated metasurface near-field distributions. a) Schematic of single meta-atom (90 nm cube, 10 nm radius of curvature on the corners, 3 nm dielectric layer), *L* is the cube size and *H* is the gap height. b) Electric field distributions on distal plane, proximal plane, and schematic of hotspots at fundamental wavelengths. c) Electric field distributions on distal plane, proximal plane, and schematic of hotspots at second harmonic wavelengths. d) Far-field scattering, absorbance, and calculated extinction spectra for the metasurface. e) Local electric field intensity in the cavity (proximal) and on the AgNC top surface (distal plane) as a function of incident wavelength; inset shows the schematics of distal plane and proximal plane.

strongly enhanced optical fields.[37] Such colloidal metasurfaces are particularly advantageous for enhanced SHG platforms because the parameters that affect field enhancement at the fundamental and second harmonic frequencies can be independently tuned.

2. Results and Discussion

A schematic of the metasurface geometry is shown in **Figure 1**a. Ag nanocubes (AgNCs) deposited onto a metal backplane forms a metal–dielectric–metal interface that serves as the structural repeat unit, or meta atom, of the SHG metasurface. Near-field enhancement at the fundamental frequency is largely dictated by the thickness of the polymer space layer due to a gap mode that results from capacitive coupling between the nanocube and the Au backplane. This gap mode (Figure 1b) is largely dependent on both spacer layer thickness (which determines gap height) and cube size (which determines gap size). Field enhancement at the second harmonic frequency stems from a localized surface plasmon resonance (LSPR) associated with the Ag nanocube (Figure 1c), and is thus primarily dictated by the size of the Ag cube. This cube mode is highly dependent on cube size, but independent of spacer layer thickness. Thus, control over the structural parameters of the colloidal metasurface allows for orthogonal control over near-field enhancement at the fundamental and second harmonic frequencies.

First, we carried out full-wave electrodynamic simulations (Lumerical FDTD Solutions) to investigate how the LSPRs of the nanocube and coupled nanocube–film architecture influence SHG enhancement. The local electric-field enhancement ($|E/E_0|$) distribution for a cross section located in the nanocube-film gap, 0.5 nm below Ag nanocube bottom surface (proximal plane) is shown in Figure 1b,c. Figure 1d plots the simulated far-field scattering (black), absorbance (red), and the calculated

extinction (blue) of the metasurface. The fundamental gap mode ($\lambda = 1060$ nm) is a source of strong optical absorption and moderate scattering. Absorptions associated with confinement of the gap mode are observed at the edges of the nanocube, and are present in the simulated absorbance as oscillations in the absorbance intensity at wavelengths just above and below the fundamental mode. The absorption and scattering peaks located between 400 and 700 nm in the simulated spectra are consistent with "isolated" LSPR modes of the Ag nanocube.[38] The broad feature at $\lambda = 500$ nm corresponds to the first-order dipole mode of the Ag nanocube, whereas the peak located near $\lambda = 420$ nm originates from the quadrupole and other higher-order LSPRs.[39] However, the field enhancement induced by the quadrupole mode is dominant over the enhancement induced by dipole modes at the SHG wavelength.[40] The field enhancement distribution for a cross section taken just above (0.5 nm) the top surface of the Ag nanocube (distal plane) and a cross section taken inside the gap (proximal plane) are shown in Figure 1e. Thus, the nanocube metasurface exhibits a clear double SPR resonance: the gap mode responsible for enhanced absorption and the nanocube LSPR responsible for emission. From the simulation of near-field distribution, we assigned the gap mode at the fundamental wavelength as a dipole mode that stems from coupling between the Ag nanocube and Au substrate. Thus, field enhancement is consistent with SHG selection rules,[41,42] where the excitation of an SH quadrupole mode results from combined photons that stem from a dipole mode at the fundamental wavelength.[43] The spatial mode overlap that occurs inside the metasurface gap between the fundamental mode and SH mode is likely a major contributor to increasing the efficiency of the SHG process.[20]

To investigate whether these two resonances can be independently tuned, we used finite-difference time-domain (FDTD) simulations to investigate metasurface dependence on nanocube size and gap height. **Figure 2** shows the resulting NIR absorption and visible scattering spectra obtained for three colloidal metasurfaces composed of i) different cube sizes with a constant gap of $H = 3$ nm; and ii) different gap heights and a constant cube edge length $L = 90$ nm. The strong scattering peak in the visible range redshifts significantly with increasing nanocube size, from $\lambda = 410$ nm for $L = 75$ nm to $\lambda = 448$ nm for $L = 105$ nm. However, optical scattering remains constant at $\lambda = 428$ nm for all three gap heights, confirming that field enhancement near λ_{SH} is completely independent of H. The strong NIR absorption response is dependent on both cube size and gap height. For increasing cube size from $L = 75$ nm to $L = 105$ nm, the absorption peak redshifts by 286 nm due to an increase in the optical cavity size. For increasing gap height from $H = 3$ nm to $H = 7$ nm, the absorption peak blueshifts 243 nm due to weaker coupling between the nanocube and Au substrate.

To fabricate the metasurfaces, colloidal Ag nanocubes were synthesized according to a modified polyol reaction, described in detail elsewhere[44] and deposited onto a supported 50 nm Au film using Langmuir–Blodgett deposition[45] (details in "Experimental Section"). Each nanocube is encapsulated in a thin (<2 nm) polymer shell, providing a nanoscale spacer layer that insulates the Ag nanocube from the underlying Au film. **Figure 3**a shows a (top-down) scanning electron microscopy (SEM) image of a metasurface fabricated with nanocubes possessing an average edge length of 89 ± 4 nm. The nanocube array has an average nanocube center-to-center spacing of 224 ± 45 nm, and a nanocube purity of >98% (particle defect

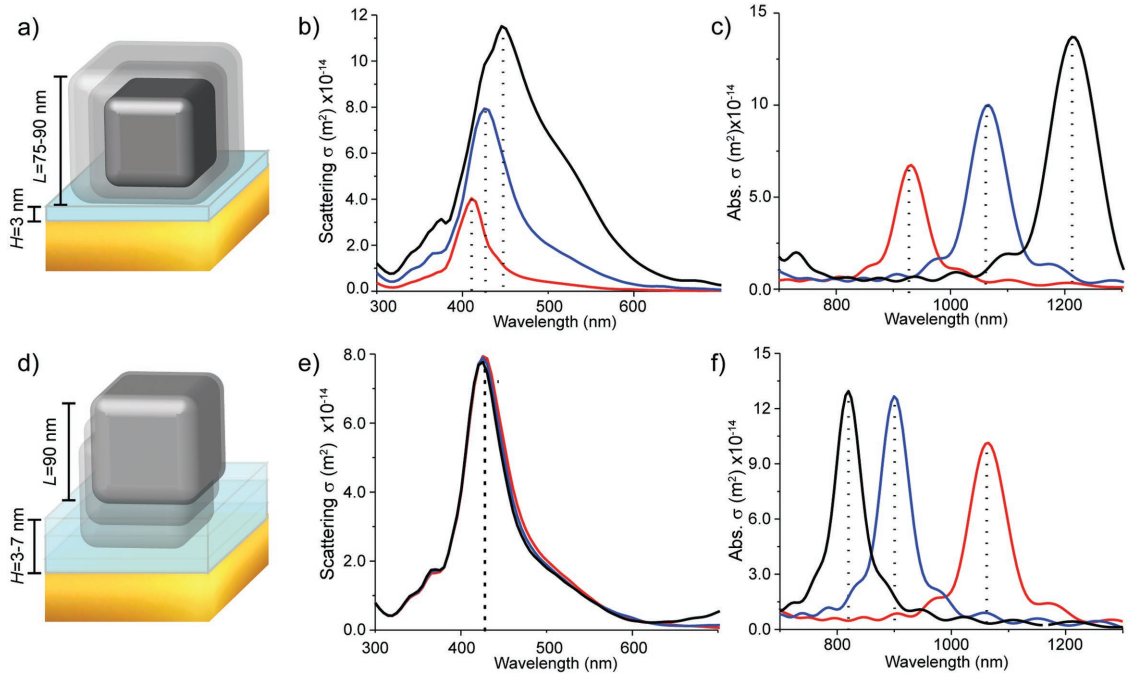

Figure 2. Simulation, dependence of gap height and cube size. a) Schematic of meta-atom made by different size of cube. b,c) Scattering and absorption cross section of metasurfaces with a constant (3 nm) gap size and varied cube size (red is 75 nm, blue is 90 nm, and black is 105 nm). d) Schematic of meta-atom made by different thickness of dielectric layer. e,f) Scattering and absorption cross section of metasurfaces with a constant (90 nm) cube size and varied gap size (red is 3 nm, blue 5 nm, and black 7 nm).

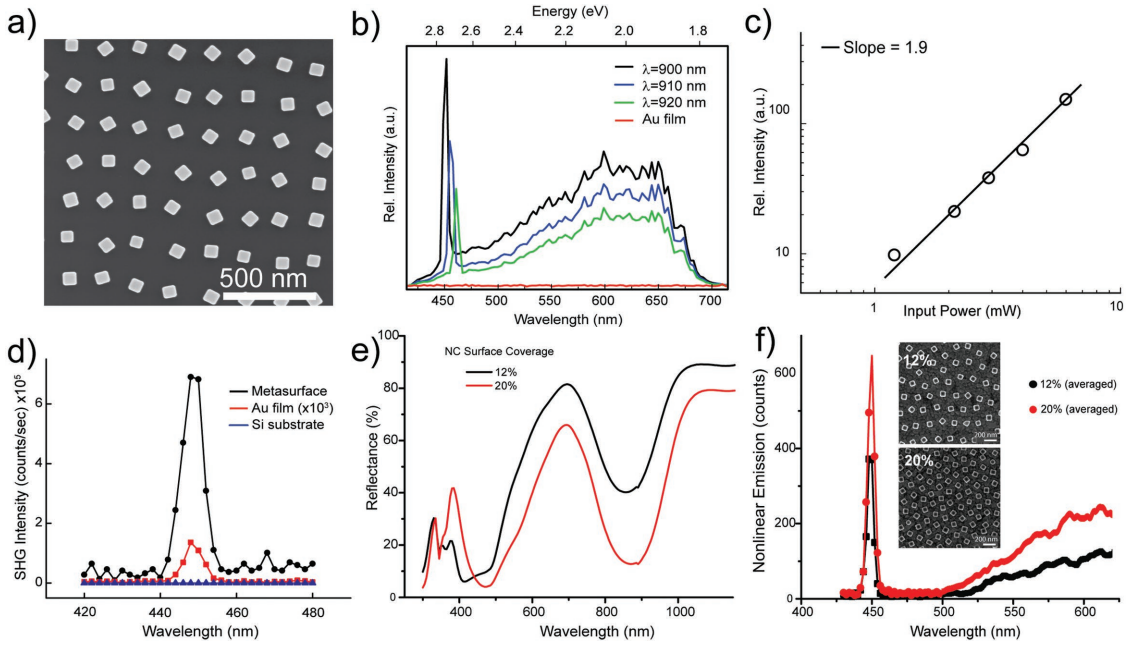

Figure 3. Wavelength, power and density dependence of metasurface second harmonic generation. a) SEM image of nanocube metasurface displaying well-spaced NC array. b) Nonlinear emission spectra from a colloidal metasurface with a fundamental gap mode at 900 nm showing λ_{FW}-dependent SHG. (corresponding reflectance spectra in Section S1 in the Supporting Information). c) SHG power dependence, showing SHG is a second-order nonlinear optical (NLO) process. d) Metasurface second harmonic enhancement factor. e) Reflectance spectra of Ag nanocube metasurfaces. f) Nonlinear emission spectra (measured with picosecond photon detection series) showing SHG at λ_{SH} = 450 nm; inset shows SEM images of two metasurfaces with different density. Panels (a)–(c) and (d)–(f) used two different batches of metasurfaces.

rate of <2%). Nanocube density and spacing can be controlled during the deposition process. A typical nonlinear optical emission spectrum for the nanocube metasurface is shown in Figure 3b (black), excited with a scanning, normal incidence pulse train at λ_{FW} = 900 nm. During excitation at the fundamental wavelength, light–matter interactions of the plasmonic structure (at the gap mode resonance) can convert the far-field E_{xy} component of the normal incident light to a near-field E_z component.[46] Plasmon excitation also promotes the interaction of the near-field with the *zzz* component of the second-order susceptibility tensor, which is strongly localized near the bottom facet of the AgNCs (inside the metasurface gap). Owing to the surface centrosymmetry broken at these metasurface junctions[41] along the *z*-direction, only the *zzz* component of the second-order susceptibility tensor is nonvanished; therefore, a significant near-field *z*-polarized coherent SHG response can be generated inside the particle-substrate gaps. The narrow SHG peak is prominent in the emission spectrum at precisely λ_{SH} = 450 nm. The other prominent feature is the expansive range of cathedral-like peaks throughout the visible spectrum from 450 to 700 nm, which we attribute to multiphoton photoluminescence; their investigation is outside the primary scope of the present work and has been reported elsewhere.[47] For comparison, the nonlinear emission from a pristine Au thin film (*sans* nanocubes) is shown with an identical illumination configuration, revealing a relatively flat and featureless spectrum (Figure 3b, red).

The nonlinear emission spectra were also recorded for optical excitation at λ_{FW} = 900, 910, and 920 nm (Figure 3b). Each spectrum exhibits a narrow second harmonic peak (full width at half maximum < 6 nm) whose position follows a strict $\lambda_{FW}/2$ dependence. Unlike this SHG peak, the broad signal attributed to multiphoton emission does not exhibit a spectral shift with varying incident wavelengths. Figure 3c shows a log–log plot of the intensity of the second harmonic peak with respect to the input power for excitation at λ_{FW} = 900 nm. Peak intensity was found to increase with a nonlinearity order of ≈1.9, which confirms the optical signal that we measured originates from a second-order nonlinear process.

In order to compare the performance of our colloidal metasurface to other SPR-based SHG platforms,[19] we calculated the SHG enhancement factor (EF). Here, we define the SHG EF as the ratio of metasurface SHG power (P_{MS}) to the SHG power of a pristine Au thin film (P_{Au}), consistent with other studies.[48] Figure 3d plots the SHG emission intensity for both the colloidal metasurface, a 75 nm Au thin film, and a 500 µm thick Si substrate, normalized to accommodate for pump power. Here, the metasurface was fabricated with Ag nanocubes (average size = 87.5 ± 3.8 nm) deposited at a surface density of 12.1%, and onto an underlying Au thin film that is 75 nm thick. For an excitation power of 3.80 mW at λ_{FW} = 900 nm, we measured the power of the SHG signal to be $P_{MS} = 2.20 \times 10^{-13}$ W. Because the unenhanced SHG signal from the bare Au film is much weaker, a higher pump power was required to detect the SHG. Using an excitation power of 264.75 mW at λ_{FW} = 900 nm, we measured the SHG power from the Au film to be $P_{Au} = 7.00 \times 10^{-14}$ W (equivalent to 1.45×10^{-17} W at 3.80 mW incident power). This gives a metasurface SHG enhancement factor of $EF_{MS} = 1.52 \times 10^4$. In addition, we did a comparison with AgNCs on a bare Si substrate. Since there is no coupling

between the AgNCs and Si, this structure serves as a single resonance structure that only exhibits a nanocube mode resonance and field enhancement at the SHG emission wavelength. As a result, the SHG efficiency of the colloidal AgNC metasurface fabricated on Au (double-resonance structure) is one order of magnitude higher than AgNCs on silicon (single resonance structure) (Section S2, Supporting Information)"

We then compared the SHG efficiencies of two colloidal metasurfaces fabricated with different nanocube densities (12% and 20%) and all other parameters the same. Figure 3e shows their near-normal specular reflectance spectra. The large dip in reflectance centered at 875 nm corresponds to the fundamental gap resonance. The spectral positions of the fundamental gap mode for both metasurfaces are similar, indicating that there is minimal interaction between the Ag nanocubes in-plane and that both metasurfaces operate within the weak interparticle coupling limit.[37] The only significant difference between the far-field response of each metasurface is the marked decrease in reflectance for the higher nanocube density. To calculate the SHG efficiency of each metasurface, we define efficiency as the ratio of the fundamental beam power to the metasurface SHG power

$$\eta_{SHG} = \frac{P_{FW}}{P_{MS}}$$

For a colloidal metasurface with a 12% nanocube density excited with $P_{FW} = 3.80 \times 10^{-3}$ W, we measured SHG efficiency to be $\eta_{SHG} = (4.87 \pm 0.28) \times 10^{-11}$, whereas for the 20% density metasurface the efficiency is $\eta_{SHG} = (8.29 \pm 1.23) \times 10^{-11}$. This 67% increase in the density of meta-atoms covering the surface leads to a 70% increase in SHG efficiency (Figure 3f) indicates the far-field emission we collected is incoherent SHG. During the emission process, near-field E_z component at fundamental frequency been converted to near-field coherent z-polarized SHG signal which confined inside junction. Then, through cube mode plasmonic resonance (at SHG frequency), near-field SHG signal emits out from junction and become incoherent far-field SHG due to the plasmonic resonance lifetime. Furthermore, owing to the aperiodic macroscopic pattern, the far-field SHG signal from different junctions has interference with poor phase matching in spatial; therefore, the overall far-field SHG signal is incoherent[49] which propagate off-(z)-axis, and collected by the aperture of the objective.

The highest efficiencies we measured were $\eta_{SHG} = 5.36 \times 10^{-9}$ (Section S3, Supporting Information) with 15.6 GW cm^{-2} peak excitation intensity (λ_{FW} = 800 nm, 0.2 s dwell time) and $\eta_{SHG} = 1.2 \times 10^{-9}$ from the same metasurface with a longer 1 s dwell time. This decrease in efficiency indicates some materials degradation of the colloidal metasurface under extended laser illumination, potentially from either oxidation of Ag or nanocrystal reshaping due to photothermal effects.[50–52] In comparison, previous reports for bowtie apertures made by lithography exhibit $\eta_{SHG} = 6.33 \times 10^{-9}$ under 0.8 GW cm^{-2}[19] and comparably $\eta_{SHG} = 1.23 \times 10^{-8}$ under 1.61 GW cm^{-2} for ultrasmooth antennas.[20] While our colloidal metasurfaces exhibit lower SHG emission efficiencies, they possess much larger device areas with the potential for high meta-atom densities and wafer-scale fabrication (see Section S4 in the Supporting Information for a detailed comparison).

Tunability of the colloidal metasurface structure also enables further investigation of the double-resonance effect. SHG enhancement is proportional to $f(\lambda_{SH})^2 \cdot f(\lambda_{FW})^4$ where f is the field strength.[53] Thus, the near-field enhancement at λ_{FW} is expected to dominate the observed SHG signal in our double-resonance structure. In a double-resonance structure, energy transfer from mode coupling (η_{rad}) has also been shown to be a crucial factor in determining SHG efficiency.[21] To investigate the relative importance of near-field enhancement versus mode coupling, we fabricated two colloidal metasurfaces that exhibit the same nanocube LSPR modes but possess different gap resonance wavelengths at λ = 890 nm (labeled M890) and λ = 1020 nm (labeled M1020).

Figure 4a,b shows the SHG excitation spectrum, which is a plot of the SHG intensity for varying fundamental excitation wavelengths between λ_{FW} = 750 and 1050 nm. Data points were obtained in 50 nm increments and normalized to the incident intensity (10 GW cm^{-2}) (Section S5, Supporting Information) and detector efficiency. The data points are fit with two overlapped Gaussian functions (Section S6, Supporting Information) to identify SHG maxima. In Figure 4a, a maximum in SHG signal intensity for M890 is obtained at λ_{FW} = 815 nm excitation, with a secondary SHG peak obtained at λ_{FW} = 884 nm and a weak but nonzero SHG signal at λ_{FW} > 1000 nm. Figure 4b shows the SHG excitation scan for M1020, where a peak in SHG emission occurs at λ_{FW} = 1029 nm, another peak located at λ_{FW} = 875 nm. Figure 4c,d shows the reflectance and absorbance for M890 and M1020, respectively. For M890, the optical resonances of the metasurface are designed to possess good overlap with λ_{FW} and λ_{SH}. For M1020, the LSPR modes of the metasurface are designed to possess poor overlap with either λ_{FW} or λ_{SH}. Figure 4e,f shows the expected SHG enhancement factors and radiation efficiencies for each metasurface. Experimental absorbance and reflectance spectra in Figure 4c,d were used to calculate the relative SHG enhancement factor $f(\lambda_{SH})^2 \cdot f(\lambda_{FW})^4$ (Section S7, Supporting Information). To validate these results, we performed finite element method simulations to obtain the wavelength-dependent radiation efficiency (blue line). These results were obtained by adding 28 dipole sources at the hotspots inside gap (Section S8, Supporting Information), this radiation efficiency corresponds to conversion of near-field SHG to far-field SHG. The radiation efficiency includes several factors, including coupling between the near-field SHG quadrupole mode, and the far-field SHG dipole mode.

For M890 (Figure 4e), the SHG enhancement factor peak (black) at λ_{FW} = 825 nm is consistent with strong SHG efficiency peak at λ_{FW} = 815 nm, and the radiation efficiency peak (blue) at λ_{FW} = 880 nm is consistent with the secondary SHG efficiency peak at 884 nm. For M1020 (Figure 4f), the SHG enhancement factor peak (black) at 1040 nm is consistent with peak in SHG emission (black) at λ_{FW} = 1029 nm, and the maximum radiation efficiency (blue) at λ_{FW} = 880 nm is consistent with another SHG efficiency peak at λ_{FW} = 875 nm. To confirm the peak identification and analysis, we fabricate another metasurface with 920 nm gap mode resonance (M920) and perform excitation scan with 25 nm data interval (Section S9, Supporting Information). Our experimental data show M920 has two SHG efficiency peaks: one peak at 825 nm

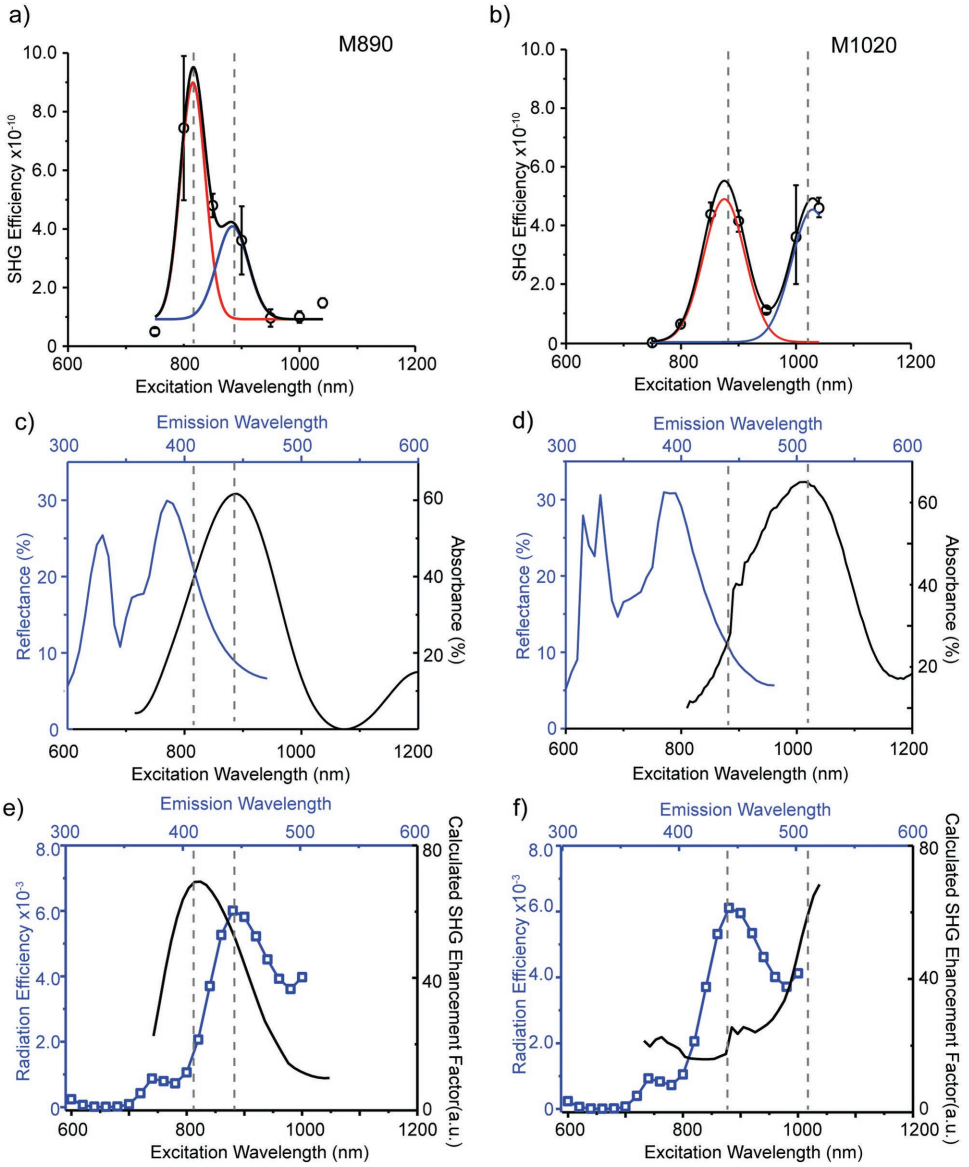

Figure 4. Linear and nonlinear optical metasurface responses. Excitation wavelength-dependent SHG efficiency of a) M890 and b) M1020, respectively; black dots are measured data points, red and blue curve are Gaussian function curve fitting. All SHG efficiency data are normalized to excitation intensity of 10 GW cm^{-2}. Experimental reflectance and absorbance spectra for metasurfaces with fundamental gap modes centered at c) 890 nm and d) 1020 nm; blue curve is reflectance measurement at emission wavelength (top axis) and black curve is absorption measurement at excitation wavelength (bottom axis). Wavelength-dependent radiation efficiency (blue curve) and calculated enhancement $f(\lambda_{SH})^2 \cdot f(\lambda_{FW})^4$ (black curve) of e) M890 and f) M1020, respectively.

consists with enhancement factor peak, another peak at 875 nm consists with radiation efficiency peak, and both peak can be fitted with the Gaussian function. As a result, we find that SHG is proportional to both SHG enhancement factor and radiation efficiency ($f(\lambda_{SH})^2 \cdot f(\lambda_{FW})^4 \cdot \eta_{rad}$).

3. Conclusions

Overall, this work demonstrates the scalable fabrication of colloidal metasurfaces for enhanced SHG platforms utilizing a double-resonance structure. We use these platforms to explore the mechanism for enhanced SHG, and determine that both near-field enhancement and mode coupling are critical parameters. By tuning meta-atom size, density, and arrangement, the field enhancement associated with both nonlinear absorption and linear scattering processes can be precisely controlled. Given the ability to synthesize metal nanocrystal with a wide variety of shapes and materials, it may be possible to greatly increase SHG efficiencies of these platforms and extend SPR-based enhancement to other nonlinear optical conversion processes. The tunability of the colloidal device structure also provides a convenient strategy for designing SHG platforms with different working frequencies, with the potential for

creating hybrid structures with multiple working frequencies on a single platform. In addition, owing to plasmonic resonance lifetime and poor phase matching in spatial, the far-field SHG signal we measured is incoherent. In the future, with proper design of the periodic colloidal metasurface by using surface functionalized AgNCs, it is possible to generate far-field spatial-coherent SHG from colloidal metasurface. Such a metasurface will enable the phase and polarization control for the further functionalization in the integrated nonlinear optics.

4. Experimental Section

Gold Substrate Fabrication: Au substrates were fabricated through sputtering (using Denton Discovery 18 Sputter System). Here, 500 µm thick, 1 cm by 1 cm size, glass substrates were washed with ethanol, piranha solution, deionized (DI) water, and dried with nitrogen stream. The sputtering radio-frequency (RF) bias was used to clean the substrate for 40 s, and followed by Cr (400 W, 5 s) and Au film (300 W, 115 s) sputtering with the Ar gas pressure as 2.4 mTorr.

AgNC Synthesis: AgNCs were synthesized via a polyol synthesis described before.[44,54] $CuCl_2$, $AgNO_3$, and 1,5-pentanediol were added to a glass vial and dissolved through sonication. In a separate glass vial, polyvinylpyrrolidone (PVP) (M_W = 55 000) was dissolved in 1,5-pentanediol. Then, 10 mL of 1,5-pentanediol was added to a 50 mL round bottom flask, heated up to 193 °C, and the precursors were injected into the hot solution. The synthesized AgNCs were vaccum-filtered (using 650, 450, and 220 nm pore size Millipore Durapore membranes) to reduce the polydispersity. The filtered AgNCs were centrifuged in ethanol to remove excess PVP and then redispersed in 15 mL ethanol for later using.

Metasurface Fabrication: About 3 mL of AgNCs was taken (stored in ethanol); 17 mL of ethanol was added; and then it was centrifuged at 3400 rpm for 15 min and redispersed in 10 mL ethanol and centrifuged at 3400 rpm for 15 min. Then, 1 mL of $CHCl_3$ was added and sonicated to fully dispersed. A glass Petri dish was filled with DI water, and AgNCs (in $CHCl_3$) were added drop by drop to the Petri dish. The more the drops added, the higher the AgNC film density achieved. After making the AgNCs film, it was waited for about 1 h and the AgNC film was transferred to the Au substrates by simply dipping into the Petri dish.

SHG Measurement with a Confocal Microscope: As shown in Figure 3b,c, back-scattering mode of Leica SP5 Confocal/MultiPhoton System (Leica Upright Microscope; 0.75 numerical aperture (NA) 20X dry objective; Leica GaAsP hybrid PMT detector) was used. A tunable Ti–Sapphire laser was used as the excitation source with ≈100 fs pulse width, 80 MHz repetition rate, and tunable emission from 690 to1040 nm.

SHG Measurement with Picosecond Photon Detection Series: A picosecond photon detection series was used for all SHG measurements except for that shown in Figure 3b,c, because it had well-calibrated count to photon number conversion efficiency, for accurate measurement of SHG emission power. The excitation laser source was MaiTai HP (100 fs pulse width and 80 MHz repetition rate, 690–1040 nm tunable wavelength); the objective lens was 20× with 0.45 NA; the microscope was Olympus IX81; the detector was Horiba PM, Picosecond Photon Detection Series.

Excitation wavelength from 750 to 1040 nm, with 50 nm increment (with the exception of a 40 nm increment between last two data points), was chosen. For each individual measurement, excitation wavelength and laser power were constant, and an emission scan was carried out using a monochromator starting at 300 nm and with a 2 nm bandwidth, 2 nm increments, and a 1 s dwell time (unless otherwise noted). Then, the total counts were calculated from $\left(\frac{\lambda_{\text{Excitation}}}{2}-5\right)$ nm to $\left(\frac{\lambda_{\text{Excitation}}}{2}+5\right)$ nm because the bandwidth of laser was roughly 10 nm. System detection efficiency at different wavelengths was calibrated with standard nonlinear crystal; the system detection efficiency was used to covert measured counts to SHG photon numbers, and then the SHG power was calculated. Excitation power at fundamental wavelength was measured with a Vega P/N 7Z01560 Power Meter.

Supporting Information

Supporting Information is available from the Wiley Online Library or from the author.

Acknowledgements

Y.Z., H.Q., and M.J.R. contributed equally to this work. The authors would like to thank the UCSD School of Medicine Microscopy Core for the use of their facility and acknowledge its supporting grant, NS047101. The authors also would like to thank the Nano3 facility at Calit2 for the use of their facility.

Conflict of Interest

The authors declare no conflict of interest.

Keywords

metasurfaces, nonlinear optics, plasmonics, second harmonic generation

Received: May 2, 2018
Revised: September 19, 2018
Published online:

[1] M. Kauranen, A. V. Zayats, *Nat. Photonics* **2012**, *6*, 737.
[2] J. Butet, P.-F. Brevet, O. J. F. Martin, *ACS Nano* **2015**, *9*, 10545.
[3] J. Butet, J. Duboisset, G. Bachelier, I. Russier-Antoine, E. Benichou, C. Jonin, P.-F. Brevet, *Nano Lett.* **2010**, *10*, 1717.
[4] Y. Zhang, N. K. Grady, C. Ayala-Orozco, N. J. Halas, *Nano Lett.* **2011**, *11*, 5519.
[5] R. Czaplicki, H. Husu, R. Siikanen, J. Mäkitalo, M. Kauranen, J. Laukkanen, J. Lehtolahti, M. Kuittinen, *Phys. Rev. Lett.* **2013**, *110*, 093902.
[6] R. W. Boyd, in *Nonlinear Optics*, Academic Press, San Diego, CA **2008**, pp. 1–67.
[7] S. S. Jha, *Phys. Rev.* **1965**, *140*, A2020.
[8] N. Bloembergen, R. K. Chang, S. S. Jha, C. H. Lee, *Phys. Rev.* **1968**, *174*, 813.
[9] F. X. Wang, F. J. Rodríguez, W. M. Albers, R. Ahorinta, J. E. Sipe, M. Kauranen, *Phys. Rev. B* **2009**, *80*, 233402.
[10] G. Bachelier, J. Butet, I. Russier-Antoine, C. Jonin, E. Benichou, P.-F. Brevet, *Phys. Rev. B* **2010**, *82*, 235403.
[11] C. Ciracì, E. Poutrina, M. Scalora, D. R. Smith, *Phys. Rev. B* **2012**, *86*, 115451.
[12] Y. Pu, R. Grange, C.-L. Hsieh, D. Psaltis, *Phys. Rev. Lett.* **2010**, *104*, 207402.
[13] Y. Zhang, A. Manjavacas, N. J. Hogan, L. Zhou, C. Ayala-Orozco, L. Dong, J. K. Day, P. Nordlander, N. J. Halas, *Nano Lett.* **2016**, *16*, 3373.
[14] P. Mühlschlegel, H.-J. Eisler, O. J. F. Martin, B. Hecht, D. W. Pohl, *Science* **2005**, *308*, 1607.
[15] C. K. Chen, T. F. Heinz, D. Ricard, Y. R. Shen, *Phys. Rev. B* **1983**, *27*, 1965.

[16] A. Bouhelier, M. Beversluis, A. Hartschuh, L. Novotny, *Phys. Rev. Lett.* **2003**, *90*, 013903.
[17] K. Thyagarajan, S. Rivier, A. Lovera, O. J. F. Martin, *Opt. Express* **2012**, *20*, 12860.
[18] H. Linnenbank, Y. Grynko, J. Förstner, S. Linden, *Light: Sci. Appl.* **2016**, *5*, e16013.
[19] S. Park, J. W. Hahn, J. Y. Lee, *Opt. Express* **2012**, *20*, 4856.
[20] M. Celebrano, X. Wu, M. Baselli, S. Großmann, P. Biagioni, A. Locatelli, C. De Angelis, G. Cerullo, R. Osellame, B. Hecht, L. Duò, F. Ciccacci, M. Finazzi, *Nat. Nanotechnol.* **2015**, *10*, 412.
[21] K. Y. Yang, J. Butet, C. Yan, G. D. Bernasconi, O. J. F. Martin, *ACS Photonics* **2017**, *4*, 1522.
[22] N. Weber, M. Protte, F. Walter, P. Georgi, T. Zentgraf, C. Meier, *Phys. Rev. B* **2017**, *95*, 205307.
[23] H. Harutyunyan, G. Volpe, R. Quidant, L. Novotny, *Phys. Rev. Lett.* **2012**, *108*, 217403.
[24] H. Aouani, M. Navarro-Cia, M. Rahmani, T. P. H. Sidiropoulos, M. Hong, R. F. Oulton, S. A. Maier, *Nano Lett.* **2012**, *12*, 4997.
[25] S.-D. Liu, E. S. P. Leong, G.-C. Li, Y. Hou, J. Deng, J. H. Teng, H. C. Ong, D. Y. Lei, *ACS Nano* **2016**, *10*, 1442.
[26] K. Thyagarajan, J. Butet, O. J. F. Martin, *Nano Lett.* **2013**, *13*, 1847.
[27] S. D. Gennaro, M. Rahmani, V. Giannini, H. Aouani, T. P. H. Sidiropoulos, M. Navarro-Cía, S. A. Maier, R. F. Oulton, *Nano Lett.* **2016**, *16*, 5278.
[28] J. Butet, O. J. F. Martin, *Opt. Express* **2014**, *22*, 29693.
[29] M. Navarro-Cia, S. A. Maier, *ACS Nano* **2012**, *6*, 3537.
[30] L. A. Lyon, D. J. Pen, M. J. Natan, *J. Phys. Chem. B* **1999**, *103*, 5826.
[31] C. J. Orendorff, T. K. Sau, C. J. Murphy, *Small* **2006**, *2*, 636.
[32] J. J. Mock, M. Barbic, D. R. Smith, D. A. Schultz, S. Schultz, *J. Chem. Phys.* **2002**, *116*, 6755.
[33] A. M. Funston, C. Novo, T. J. Davis, P. Mulvaney, *Nano Lett.* **2009**, *9*, 1651.
[34] M. Airola, Y. Liu, S. Blair, *J. Opt. A: Pure Appl. Opt.* **2005**, *7*, S118.
[35] J. Lee, N. Nookala, J. S. Gomez-Diaz, M. Tymchenko, F. Demmerle, G. Boehm, M.-C. Amann, A. Alù, M. A. Belkin, *Adv. Opt. Mater.* **2016**, *4*, 664.
[36] A. Moreau, C. Ciracì, J. J. Mock, R. T. Hill, Q. Wang, B. J. Wiley, A. Chilkoti, D. R. Smith, *Nature* **2012**, *492*, 86.
[37] M. J. Rozin, D. A. Rosen, T. J. Dill, A. R. Tao, *Nat. Commun.* **2015**, *6*, 7325.
[38] J. M. McLellan, Z. Y. Li, A. R. Siekkinen, Y. Xia, *Nano Lett.* **2007**, *7*, 1013.
[39] O. Nicoletti, F. de la Peña, R. K. Leary, D. J. Holland, C. Ducati, P. A. Midgley, *Nature* **2013**, *502*, 80.
[40] F. Zhou, Z.-Y. Li, Y. Liu, Y. Xia, *J. Phys. Chem. C* **2008**, *112*, 20233.
[41] J. I. Dadap, J. Shan, K. B. Eisenthal, T. F. Heinz, *Phys. Rev. Lett.* **1999**, *83*, 4045.
[42] J. Butet, G. Bachelier, I. Russier-Antoine, C. Jonin, E. Benichou, P. F. Brevet, *Phys. Rev. Lett.* **2010**, *105*, 1.
[43] J. Butet, I. Russier-Antoine, C. Jonin, N. Lascoux, E. Benichou, P. F. Brevet, *Nano Lett.* **2012**, *12*, 1697.
[44] Y. Sun, Y. Xia, *Science* **2002**, *298*, 2176.
[45] M. C. Petty, *Langmuir–Blodgett Films: an Introduction*, Cambridge University Press, Cambridge **1996**.
[46] J. Lee, M. Tymchenko, C. Argyropoulos, P.-Y. Chen, F. Lu, F. Demmerle, G. Boehm, M.-C. Amann, A. Alù, M. A. Belkin, *Nature* **2014**, *511*, 65.
[47] O. Demichel, M. Petit, S. Viarbitskaya, R. M??jard, F. De Fornel, E. Hertz, F. Billard, A. Bouhelier, B. Cluzel, *ACS Photonics* **2016**, *3*, 791.
[48] J. B. Lassiter, X. Chen, X. Liu, C. Ciracì, T. B. Hoang, S. Larouche, S. H. Oh, M. H. Mikkelsen, D. R. Smith, *ACS Photonics* **2014**, *1*, 1212.
[49] E. A. Mamonov, T. V. Murzina, I. A. Kolmychek, A. I. Maydykovsky, V. K. Valev, A. V. Silhanek, E. Ponizovskaya, A. Bratkovsky, T. Verbiest, V. V. Moshchalkov, O. A. Aktsipetrov, *Opt. Lett.* **2011**, *36*, 3681.
[50] S. Link, Z. L. Wang, M. A. El-Sayed, *J. Phys. Chem. B* **2000**, *33*, 7867.
[51] L. Tong, C. M. Cobley, J. Chen, Y. Xia, J.-X. Cheng, *Angew. Chem., Int. Ed.* **2010**, *49*, 3485.
[52] H. Petrova, J. Perez Juste, I. Pastoriza-Santos, G. V. Hartland, L. M. Liz-Marzán, P. Mulvaney, J. M. Penisson, A. Bourret, *Phys. Chem. Chem. Phys.* **2006**, *8*, 814.
[53] S.-J. Ding, F. Nan, D.-J. Yang, Y.-T. Zhong, Z.-H. Hao, Q.-Q. Wang, *Nanoscale* **2015**, *7*, 15798.
[54] T. J. Dill, M. J. Rozin, S. Palani, A. R. Tao, *ACS Nano* **2016**, *10*, 7523.